Current Applied Physics 13 (2013) 1558–1565

Contents lists available at SciVerse ScienceDirect

Current Applied Physics

journal homepage: www.elsevier.com/locate/cap

Solvent effect on the optimization of 1.54 μm emission in Er-doped Y_2O_3–Al_2O_3–SiO_2 powders synthesized by a modified Pechini method

A.C. Mendes [a,*], L.J.Q. Maia [b], E.C. Paris [c], M. Siu Li [a]

[a] Instituto de Física de São Carlos, Universidade de São Paulo, P.O. Box 369, São Carlos, SP, Brazil
[b] Instituto de Física, Universidade Federal de Goiás, P.O. Box 131, Goiânia, GO, Brazil
[c] Empresa Brasileira de Pesquisa Agropecuária, Embrapa Instrumentação, Rua XV de novembro 1452, 14801-970 São Carlos, SP, Brazil

ARTICLE INFO

Article history:
Received 13 December 2012
Received in revised form
25 May 2013
Accepted 10 June 2013
Available online 26 June 2013

Keywords:
Nanopowders
Yttrium aluminosilicates
Pechini method
Photoluminescence

ABSTRACT

In order to find a new Er-doped host for near infrared (NIR) optical amplifiers, a study on the optimization of the erbium emission ions in the Y_2O_3–Al_2O_3–SiO_2 system was performed. $(100 - x)\ Y_3Al_5O_{12} - (x)\ SiO_2$ powders (x varies from 0 to 70, in mol%) with a fixed Er_2O_3 concentration of 1.0 mol% were synthesized by a modified Pechini method and heat-treated at 900 and 1000 °C. The photoluminescence (PL) spectra at 1540 nm of the $^4I_{13/2} \rightarrow {}^4I_{15/2}$ transition of Er^{3+} ions and the up-conversion spectra at visible region ($^2H_{11/2} + {}^4S_{3/2} + {}^4F_{9/2} \rightarrow {}^4I_{15/2}$) upon 980 nm excitation were evaluated. Different techniques, such as thermogravimetry (TG), differential scanning calorimetry (DSC), X-ray powder diffractometry (XRD) and Fourier transform infrared spectroscopy (FT-IR) were considered to evaluate crystallization and phase-evolution of the powders as a function of the silica content (x) and annealing temperature. The analyses were based on the comparison between two different solvents used in the preparation of the polymeric resins: ethanol and water. The optimal conditions for ethanol are quite different than the conditions for water used as solvent, confirming that the PL properties at the NIR region are highly sensitive to the changes in the host stoichiometry and processing conditions. The highest emission intensity at 1540 nm was observed for $x = 30$ for ethanol and $x = 70$ for water, treated at 900 and 1000 °C, respectively. This result could be attributed to the combination of low symmetry and good dispersion of the Er^{3+} ions in these hosts.

1. Introduction

Rare-earth-doped materials play important roles in optoelectronic technology because they have good performance in a variety of optical devices such as amplifiers, waveguides, display materials and solid state lasers [1]. In the case of free rare-earth (RE) ions, the optical emission of internal 4f-4f transitions is forbidden by electric dipole [2,3]. If the symmetry of the local crystal field around the RE lattice sites in the host matrix is distorted, the parity forbidden intra-4f transition will be allowed resulting in photons of characteristic frequencies over a wide band of the electromagnetic spectrum. Among these RE elements, the 1.54 μm photoluminescence properties of trivalent erbium ions are key elements in fiber optical communication systems, because the radiative transition $^4I_{13/2} \rightarrow {}^4I_{15/2}$ of Er^{3+} ions matches the lowest signal attenuation in silica-based optical fibers [4].

A logical next step in optical amplifiers development is the planar amplifier, in which Er-doped channel waveguides are made on planar substrates. Given the small length of a planar amplifier, a higher Er^{3+} ion concentration is required. At such high concentrations, ion–ion interactions reduce the PL efficiency due to the low solubility of the rare-earth dopant ion in silica glass. The optimal concentration of Er_2O_3 in pure SiO_2 sol–gel glass is equal to 0.65 mol% [5]. Such a low value limits their use in NIR applications.

Yttrium aluminate and yttrium aluminosilicate (YAS), usually glasses, are known for their ability to accommodate high concentration of erbium active ions and for their low phonon energy due to the aluminate network [6]. In addition, these compositions are very interesting from the structural point of view. Different phases of the Y_2O_3–Al_2O_3 system are known according to the molar ratio and thermodynamic condition, namely: yttrium aluminum with a garnet structure – YAG ($Y_3Al_5O_{12}$, with $Y_2O_3/Al_2O_3 = 3{:}5$), monoclinic structure – YAM ($Y_4Al_2O_9$, with $Y_2O_3/Al_2O_3 = 2{:}1$), perovskite YAP and hexagonal YAH ($YAlO_3$, both with $Y_2O_3/Al_2O_3 = 1{:}1$. In this

* Corresponding author. Tel./fax: +55 16 33738085x212.
E-mail addresses: alecarlausp@yahoo.com.br, alessandra@ursa.ifsc.usp.br (A.C. Mendes).

1567-1739/$ – see front matter © 2013 Elsevier B.V. All rights reserved.
http://dx.doi.org/10.1016/j.cap.2013.06.012

case, a cubic phase can also be observed) [7]. The addition of silica, a typical glass forming, to this system can change the local structure and thus significantly alter their properties.

The Pechini method is well-known and used for the synthesis of optical multicomponent oxide materials. This method includes a combined process of metal complex formation and polymerization of organics, frequently used as the alternative to the metal-alkoxides based sol–gel process [8]. This soft chemistry process is advantageous because it involves better chemical homogeneity, smaller particle sizes and low synthesis temperatures of compositions with unique properties into powder, thin films and monolithic forms [9]. However, this process has some intrinsic disadvantages, for instance, the nonradiative relaxation channels due to RE concentration quenching and vibrations of hydroxyl groups (OH^-) [10].

In the present paper we describe the host effect on the PL properties in Er-doped yttrium aluminosilicate powders prepared by a modified Pechini method, using water and ethanol as the solvents. The influence of hosts with different stoichiometries on the excited-state $^4I_{13/2}$ of Er^{3+} ions was investigated in heat-treated Y_2O_3–Al_2O_3–SiO_2 powders. Up-conversion effect was also evaluated in order to find the conditions that optimize the emission intensity at 1540 nm. The nanopowders morphology was investigated by field emission gun scanning electron microscope (FEG-SEM). The effects of the silica concentration, annealing temperature and the kind of solvent on the structure of the powders were studied by X-ray powder diffractometry (XRD) and Fourier transform infrared spectroscopy (FT-IR). The thermal properties were analyzed by thermogravimetry (TG) and differential scanning calorimetry (DSC) curves.

2. Experimental

2.1. Samples preparation

The composition considered for the powders was: $(100 - x)$ $Y_3Al_5O_{12} - (x)$ SiO_2, with a fixed Er^{3+} concentration of 1 mol%. The silica content (x) varied systematically from 0 to 70 mol% and the Y_2O_3/Al_2O_3 molar ratio was kept equal to 3:5. Nominal sample compositions are listed in Table 1. In this table, in order to facilitate the recognition of the powders' composition, a notation was used: the letter E (or W) refers to the use of ethanol (or water) as the solvent in the preparation of the resins and the number in parenthesis following the letter E (or W) indicates the mol% of SiO_2 (also represented by x).

The synthesis of the ceramic powders was carried out by a modified polymeric precursor method (Pechini) based on the complexation of metal cations by a carboxylic acid (citric acid), followed by a polymerization process using a polyalcohol [ethylene glycol (EG)] to form a polymeric network. According to the stoichiometry of $Y_3Al_5O_{12}$ (Table 1), proper amount of the corresponding Y^{3+}, Al^{3+} and Er^{3+} nitrates ($Y(NO_3)_3{\cdot}6H_2O$, Aldrich 99.9% – $Al(NO_3)_3{\cdot}9H_2O$, Aldrich 98% – $Er(NO_3)_3{\cdot}5H_2O$, Aldrich 99.9%) were dissolved in alcoholic (or aqueous) solution of anhydrous citric acid ($C_6H_8O_7$, Qhemis 99%). The citric acid/metal mass proportion was 3:1. TEOS (tetraethoxysilane, $Si(OC_2H_5)_4$, Aldrich 98%) was used as the silicon alkoxide precursor, representing the sol–gel part of the synthesis. Separately, TEOS was first mixed with deionized water for a pre-hydrolysis (the molar ratio of TEOS: $H_2O = 1:2$) and then mixed into the metallic citrate solution (alcoholic or aqueous). EG was added in the mass ratio of citric acid/EG of 3:2. This solution was vigorously stirred at room temperature in order to ensure the hydrolysis and polycondensation of TEOS. The final solutions were aged at room temperature for one day and then kept under constant agitation at 80–90 °C to favor the reaction of polyesterification followed by evaporation of the excess solvent. The resulting resin was calcined at 150 °C/12 h, 400 °C/6 h and then at 700 °C/12 h, with a heating rate of 10 °C/min. To obtain the crystalline phases, portions of the as-obtained powders were treated at the range of 800–1000 °C using conventional furnace. A schematic representation of the synthesis process can be seen in Fig. 1.

Table 1
Nominal composition (in mol%) of the powders prepared by a modified Pechini method. The letter E (or W) refers to the use of ethanol (or water) as solvent and the number in parentheses indicates the mol% of SiO_2.

Sample		Composition (mol%)			
Ethanol as solvent	Water as solvent	Y_2O_3	Al_2O_3	SiO_2	Er_2O_3
E(0)	W(0)	37.1	61.9	0	1
E(10)	W(10)	33.4	55.6	10	1
E(20)	W(20)	29.6	49.4	20	1
E(30)	W(30)	25.9	43.1	30	1
E(50)	W(50)	18.4	30.6	50	1
E(60)	W(60)	14.6	24.4	60	1
E(70)	W(70)	10.9	18.1	70	1

2.2. Sample characterization

Photoluminescence spectra were collected at room temperature upon excitation of 980 nm of a diode laser with a usual setup consisting of a three-grating monochromator, chopper, lock-in and a photomultiplier for visible detection and a germanium (Ge) detector for NIR detection. The population decay rate (lifetime τ) at 1540 nm ($^4I_{13/2} \rightarrow {}^4I_{15/2}$ transition of Er^{3+} ions) was measured by exciting the samples with a pulsed 980 nm diode laser. The signal was detected by a Ge photodetector and was recorded using a storage digital oscilloscope.

Phase identification of the samples was performed by XRD in a 2θ range from 5 to 70° with a step of 0.020°, at a scanning speed of 2 °min^{-1}, at room temperature using CuKα radiation (Shimadzu, XRD-600). The position of the peaks and their relative intensities were compared to standard JCPDS (Joint Committee on Powder Diffraction Standards) files. The infrared spectra were recorded on an FT-IR system (Smiths Detection) equipped with an infrared-attenuated total reflectance (ATR) accessory. The FT-IR spectra were taken in the region of 650–4000 cm^{-1} with resolution of 10 cm^{-1}.

TG and DSC analysis of the powders were performed using a Netzsch Cell-STA409 analyzer from room temperature to 1100 °C. The samples were loaded in alumina crucibles and heated at 10 °C min^{-1} under air atmosphere.

A Jeol JSM-7500F field emission gun scanning electron microscope (FEG-SEM) was used to investigate the microstructure of the heat-treated powders.

3. Results and discussion

3.1. Morphology of the powders

Fig. 2 shows the FEG-SEM micrographs of E(30) and E(50) powders after thermal treatment at 700 and 1000 °C. The micrographs clearly indicated that the nanocrystallites had remarkable agglomeration, a typical feature of Pechini process. When heat-treated at 700 °C, the micrographs (Fig. 2(a) and (b)) showed aggregated particles with an average size of around 30 nm. The aggregation increased with the increasing of the annealing temperature, as a result of the intense combustion of organics used in the resin synthesis procedure. It is interesting to note the porous structure of the E(50) powder heat-treated at 1000 °C, as can be seen in Fig. 2(d), which is a result of the removal of the alcohol and water by-products of the hydrolysis and polycondensation of TEOS [11].

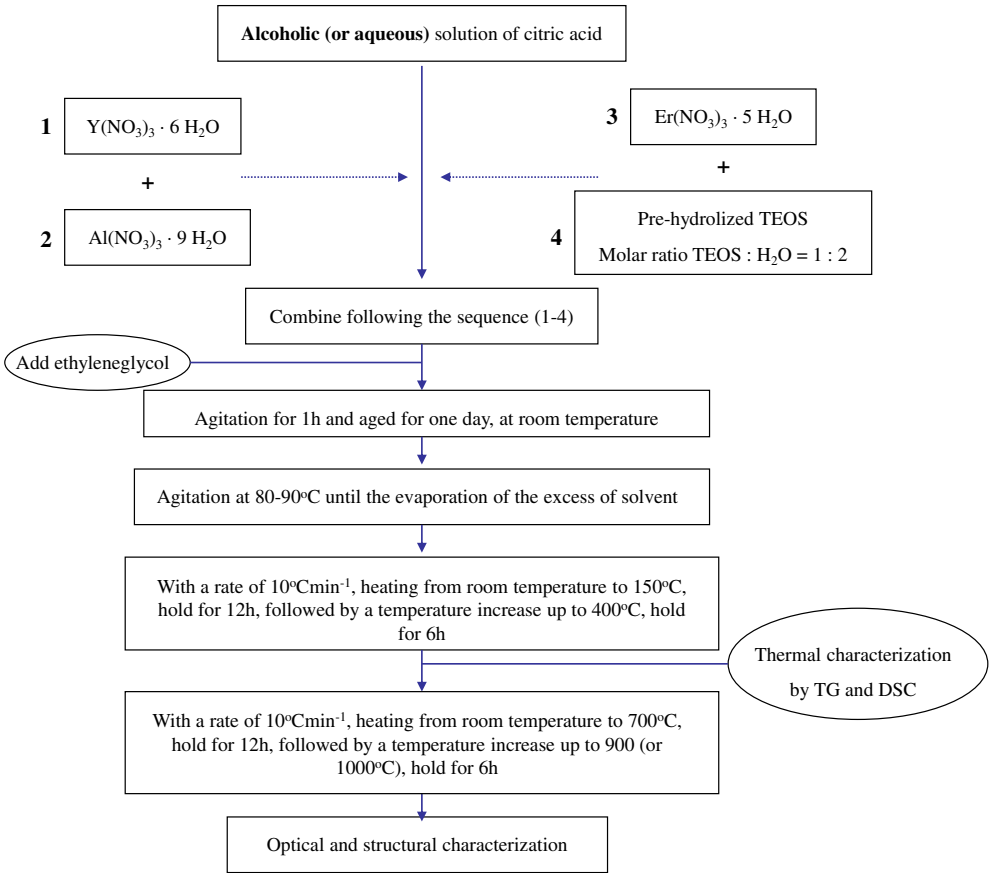

Fig. 1. Flow chart for the preparation of the powders by a modified Pechini method.

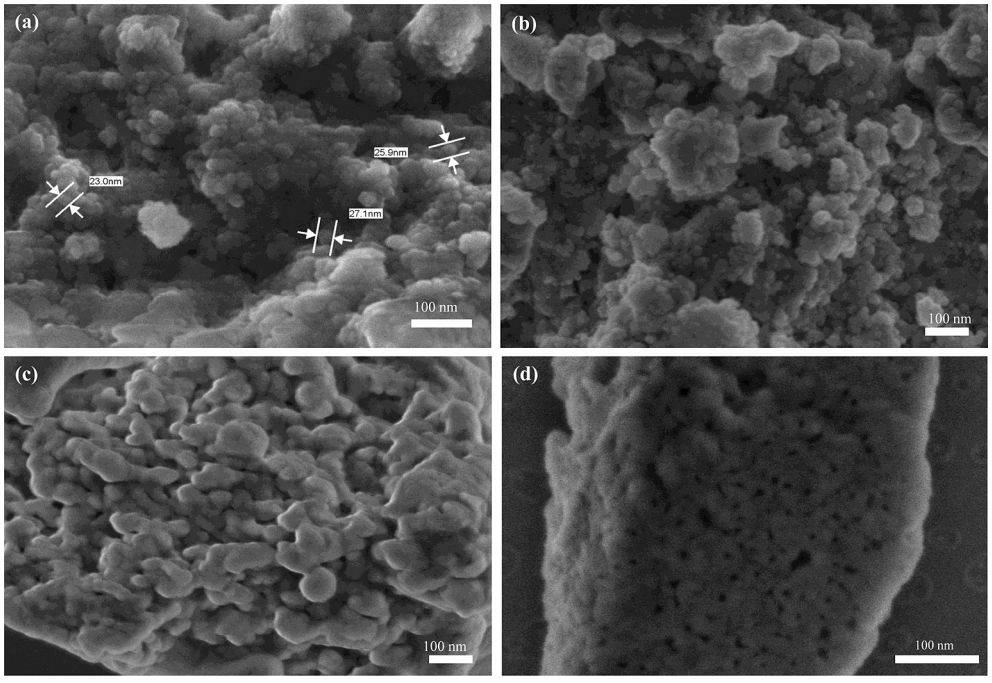

Fig. 2. FEG-SEM micrographs of (a) E(30) and (b) E(50) heat-treated at 700 °C, (c) E(30) and (d) E(50) heat-treated at 1000 °C.

3.2. Photoluminescence characterization at 1540 nm as a function of x and T

In order to find a host that optimizes the emission of Er^{3+} ions, the first stage of the present study was to investigate the PL of the powders at room temperature. It is interesting to note that all the following analyses were based on the comparison between the two different solvents used in the preparation of the polymeric resins: ethanol and water.

Fig. 3 presents the PL spectra corresponding to the $^4I_{13/2} \rightarrow {}^4I_{15/2}$ transition of Er^{3+} ions obtained upon continuous wave (CW) excitation at 980 nm for (a) E ($x = 0$–70) and (b) W ($x = 0$–70) heat-treated at 1000 °C. In order to facilitate the recognition of annealing temperature, a sample with different mol% of SiO_2 (x), heat-treated at 1000 °C, for example, was denoted as "E (x) 1000 °C or W (x) 1000 °C", where E = ethanol and W = water.

It is easy to see that the PL intensity emission at 1540 nm (I_{max}) depends on x and the kind of the solvent. The numeric values of I_{max} for all the considered samples, heat-treated at 900 and 1000 °C, can be seen in Table 2. From this table, considering E(0–70) samples, the highest I_{max} was reached for E(30) at 900 °C, while at 1000 °C it was reached for E(60). In this case, I_{max} E(30) 900 °C > I_{max} E(60) 1000 °C. Therefore, besides the dependence on x and the solvent, I_{max} also depends on the annealing temperature (T). This dependence could also be observed for W(0–70) samples, the highest I_{max} being reached for W(70) 1000 °C. So, the conditions (x and T) that optimized the intensity at 1540 nm using ethanol ($x = 30$ and $T = 900$ °C) were different from water ($x = 70$ and $T = 1000$ °C).

Some qualitative aspects could be inferred from Fig. 3 with respect to the inhomogeneous broadening of the PL spectra. In both cases [Fig. 3(a) and (b)], decreasing the content of silica, the broad PL emission (which consists of the main peak at 1540 nm and some broad shoulders) splited into many sharp bands centered at 1480, 1577, 1622 and 1650 nm. When ethanol was used as the solvent, this transition was evident when $x = 20 \rightarrow 10$. All the peaks were assigned to the f–f transitions of Er^{3+} as a result of the degeneracy-lift effect of the host crystal field that splits the levels $^4I_{13/2}$ and $^4I_{15/2}$. Due to the thermal vibration of the crystal lattice (nonradiative loss of energy) at room temperature, some transitions with emission wavelength close to 1540 nm happen synchronously and make the emission bands broaden. It is well-known that the main reason for the broadening of the PL spectrum is the local crystal field symmetry (as well as bond length and angle) at the rare-earth ion site. For this reason, when the Er^{3+} ions are embedded in an ordered crystalline structure, the spectrum shows finger patterns as a result of well-defined Stark transitions. On the other hand, rare-earth ions embedded in a disorder network exhibit a broad inhomogeneous spectrum. This broadening was represented quantitatively by the parameter "Full Width at Half Maximum (FWHM)" of the peak at 1540 nm and can be seen in Table 2 for the considered powders. The FWHM values, for the most of the samples, were 50 nm. Variations of this value were more pronounced for samples with low silica concentrations ($x = 0$–20) due to the transition of a broad PL emission into a finger pattern. This value is comparable to other compositions, usually glasses, as tellurite (65 nm), germanate (42 nm), phosphate (37 nm), other silica-based (46 nm) and higher than Er-doped silica glass (11–35 nm) [12–15].

Table 2
PL intensity at 1540 nm (I_{max}), the spectral bandwith (FWHM) of the NIR emission band and the lifetime (τ) of the level $^4I_{13/2}$ as a function of x, T and the kind of solvent.

Sample	$I_{max} \times 10^{-3}$		FWHM (nm)		τ (ms)	
	900 °C	1000 °C	900 °C	1000 °C	900 °C	1000 °C
E(0)	2.6	2.9	71	72	5.2	n.m.
E(10)	6.3	5.1	25	23	5.3	n.m.
E(20)	8.7	6.8	51	53	5.2	n.m.
E(30)	16.8	9.5	55	50	5.2	5.2
E(50)	5.8	Sample melts	52	Sample melts	5.1	Sample melts
E(60)	4.8	11.8	53	53	5.3	n.m.
E(70)	4.5	10.2	52	53	5.0	5.2
W(0)	4.8	6.1	70	70	n.m.	5.3
W(10)	4.2	5.0	13	26	n.m.	5.1
W(20)	7.9	5.8	36	25	n.m.	5.1
W(30)	9.5	10.7	53	31	5.2	5.0
W(50)	9.9	12.0	52	53	n.m.	5.1
W(60)	8.0	12.2	53	31	n.m.	5.3
W(70)	6.0	14.1	56	52	5.0	5.2

n.m. = not measured.

According to the above results, we could conclude that the PL properties at the NIR region were highly sensitive to the changes in host stoichiometry (dependence on x) and processing conditions (dependence on T and the kind of the solvent) [16].

3.3. Structural characterization: crystallinity and phase-evolution as a function of x and T

The optical properties discussed above could be satisfactorily explained in terms of structural properties, since we inferred previously that crystallization might be associated to the variations of the I_{max} and FWHM values as a function of x and T. In this context, Fig. 4 shows the XRD patterns of the powders to illustrate the effect of x on the structural evolution and the corresponding effect of

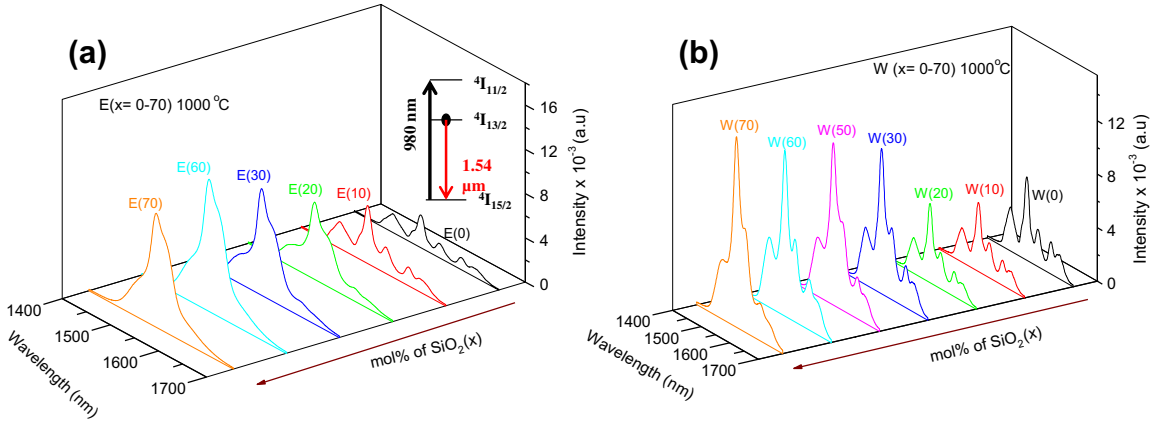

Fig. 3. Room temperature PL spectra of the $^4I_{13/2} \rightarrow {}^4I_{15/2}$ transition of Er^{3+} ions under excitation of 980 nm for (a) E ($x = 0$–70) and (b) W ($x = 0$–70), both heat-treated at 1000 °C.

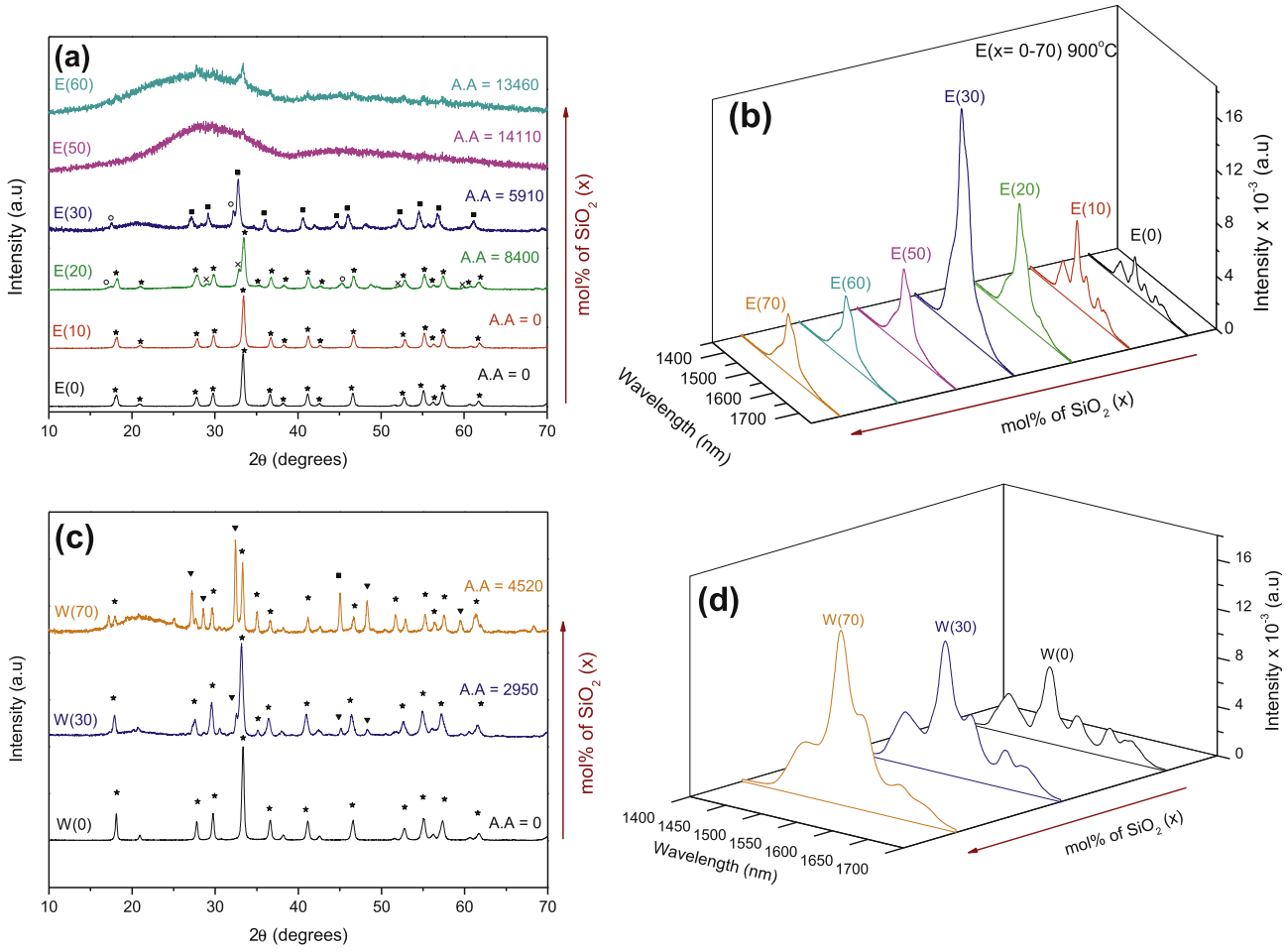

Fig. 4. XRD patterns of the (a) E ($x = 0$–70) 900 °C powders and (b) the corresponding NIR PL spectra upon excitation at 980 nm. The same analysis was considered on (c) and (d) for W(x) 1000 °C powders. The arrows, shown in all cases, indicate the increasing of silica content (x). The secondary phases indexed by symbols in the XRD patterns are listed in Table 3. *A.A* represents the "*amorphous area*", a parameter associated to the crystallinity of the samples.

crystallization on the PL spectra, taking into account the two different solvents: ethanol (a–b) and water (c–d). In this figure, we considered the conditions that optimize the intensity at 1540 nm for ethanol ($T = 900$ °C) and for water ($T = 1000$ °C).

2Considering low silica concentrations, for both water and ethanol, a well-defined crystalline phase could be clearly identified as YAG. Thus, we could infer that most of the Er^{3+} ions were located on the well-defined sites of the YAG phase and, consequently, the Stark transitions were well-defined in the PL spectra. When $x \geq 50$ (for ethanol) the host exhibited an amorphous structure. A broad band centered at $2\theta = 22°$ was observed, which is identical to the standard XRD pattern for amorphous SiO_2 (JCPS file 29-0085). In the case of water, this phenomenon was not observed even for x equal to 70, indicating that the use of water as the solvent favored the crystallization. As a result of the increase of x, the first point to note was the appearance of secondary phases (polymorphic phases of the Y_2O_3–Al_2O_3 system), for both water and ethanol. To facilitate the visualization of the secondary phases, the peaks were indexed by symbols, listed in Table 3. The second point was that these samples were partially crystalline. The corresponding diffractograms were deconvoluted into several bands. The integrated area of these bands could be quantitatively correlated to the amorphous portion in the sample and was adopted with a parameter associated to the crystallinity. The values of this parameter called as "*amorphous area (A.A)*" are presented in Fig. 4 for the considered samples. An examination of Fig. 4(a) and (c) revealed that the increase of x favored the appearance of secondary phases followed by the crystallinity decreasing. To evaluate the influence of the heat treatment temperature, the values of *A.A*, as well as the identified crystalline phases, were listed in Table 3 for the samples heat-treated at 900 and 1000 °C. The data of Table 3 show that the increase of T favors the crystallinity increasing as well as the appearance of secondary phases.

Correlating the XRD and PL results, we could infer that the crystallinity and the presence of secondary phases (both dependents on x and T) were two important and competitive parameters in the optimization of the PL intensity at 1540 nm. The optical properties of the Er^{3+} ions were optimized when there was equilibrium between these parameters. For ethanol, this equilibrium was reached when $x = 30$ and $T = 900$ °C, while for water $x = 70$ and $T = 1000$ °C.

In attempting to understand the difference between the crystallization process by using water and ethanol as the solvents, Fig. 5 shows the TG and DSC curves for powders pre-treated at 400 °C. The mass loss curves combined with the presence of exo- and endothermal events were related to the crystallization phenomena.

For powders with no silica ($x = 0$, both water and ethanol), the TG curves of Fig. 5 show that much of the mass loss takes place up to 500 °C, which could be attributed to the removal of molecular water and decomposition of partial carbonates and hydroxides contained in the precursors. In this case, the appearance of an exothermic peak at around 800 °C in the DSC curves was presumed to be caused by

Table 3
Phase-evolution, secondary phases and the values of *A.A* (*amorphous area*) as a function of *x*, *T* and the kind of solvent. The parameter *A.A* is associated to the crystallinity of the samples.

Sample	900 °C	1000 °C
E(0)	YAG Trace: Totally crystalline *Amorphous area* = 0	YAG Trace: Totally crystalline *Amorphous area* = 0
E(10)	YAG Trace: Totally crystalline *Amorphous area* = 0	YAG Trace: Totally crystalline *Amorphous area* = 0
E(20)	YAG Trace: YAH, SEC_1 *Amorphous area* = 8400	YAG Trace: YAH, SEC_2 *Amorphous area*
E(30)	SEC_3 Trace: YAH, SEC_1 *Amorphous area* = 5910	YAG Trace: SEC_1, SEC_2, SEC_3 *Amorphous area* = 4900
E(50)	Amorphous *Amorphous area* = 14,110	Sample melted
E(60)	Amorphous *Amorphous area* = 13,460	YAG + amorphous Trace: partial-crystalline *Amorphous area* = 3050
E(70)	Amorphous *Amorphous area* = n.m.	Amorphous *Amorphous area* = 9080
W(30)	SEC_3 Trace: YAH *Amorphous area* = 6290	YAG Trace: SEC_2, SEC_3 *Amorphous area* = 2950
W(70)	YAH Trace: SEC_3 *Amorphous area* = 6440	YAG Trace: SEC_1, SEC_2 *Amorphous area* = 4520

YAG (★) = $Y_3Al_5O_{12}$; YAH (×) = $YAlO_3$ (Hexagonal phase); SEC_1 (○) = $Y_3Al_2(AlO_4)_3$. SEC_2 (▼) = $Y_5Si_4Al_2O_{17}N$; SEC_3 (■) = $YAlO_3$ (Cubic phase); n.m. = not measured.

crystallization, since no mass loss was detected in these cases. The second peak, at ~900 °C, could be associated to a phase separation, said to proceed by nucleation and growth mechanisms characteristics of Y_2O_3–Al_2O_3 systems [17], which justified the appearance of secondary phases in XRD results. A very similar behavior was seen for the W(30) sample. Adding SiO_2 up to 70 mol%, the mass loss occurred until ~800 °C, probably due to the higher concentration of organics and higher porosity resulting from the hydrolysis and polycondensation of higher TEOS content.

From DSC curves, for $x = 70$, no crystallization peak was observed, for both water and ethanol. However, according to XRD results, the W(70) powder was already crystalline at 900 °C. This result could be associated to a limitation of the TG/DSC equipment that could not detect crystallization in a very small content of sample (due to the larger mass loss ~50% up to 800 °C). For $x = 30$, the crystallization appeared to begin at lower temperatures when water is used as the solvent (800 °C compared to 830 °C for ethanol). This result extended to the other compositions that were not presented in Fig. 5. So, we could conclude that the use of water as solvent favored the occurrence of crystallization at lower temperatures, in agreement with XRD results.

To complete the structural characterization, IR analysis of the synthesized samples was performed to gain more insight into the structure and composition of the powders with low crystallinity. Fig. 6 illustrates the FT-IR spectra of powders (considering $x = 0$, 30 and 70) heat-treated at 1000 °C for (a) ethanol and (b) water used as the solvents. Based on the conditions that optimized the intensity at 1540 nm, the spectrum of E(30) 900 °C was also considered. Bands at about 695, 725 and 790 cm^{-1} represent characteristic metal-oxygen (Y–O and Al–O) vibrations [18], more evident in low silica compositions, characterizing a structure dominated by aluminate formers. W (30)1000 °C showed a very similar spectrum to W (0), in agreement with the XRD and DSC results, where the use of water as solvent favored the crystallization. Bands in the spectral region of 850–1100 cm^{-1} were assigned to antisymmetric stretching vibrations of the bridging Si–O–Si bonds within (SiO_4) tetrahedral [19]. The band at 1080 cm^{-1} was very evident for high-silica powders ($x \geq 50$), characterizing a structure dominated by contributions of silica. No absorption band in the 3000–3450 cm^{-1} region (the O–H stretching vibration) was observed, implying that the heating at 900 and 1000 °C was sufficient to eliminate the hydroxyl group. It is interesting to note that a small band, at about 930–940 cm^{-1}, was only seen in the spectra of compositions that exhibit the highest values of I_{max} [E(30) and W(70)]. Kohli et al. [20] attributed this band to the non-bridging oxygen in silicon (SiO_4) tetrahedral. The importance of this result is discussed in the next section.

3.4. Nonradiative mechanisms as a function of x and T

The changes observed on I_{max} with the change of host nature might be associated to the nonradiative relaxation rate (W_{nr}). It is well established that hosts with lower phonon energy exhibit lower nonradiative loss of energy. Increasing the silica content ($x \geq 50$), the highest phonon energy increased from 930 to 1080 cm^{-1} for ethanol and from 785 to 1080 cm^{-1} for water-powders (according to the frequencies of the bands in the FT-IR spectra of Fig. 6). Consequently, silica-rich powders exhibited higher nonradiative loss of energy.

The population decay rate (lifetime) is a parameter that presents a strong dependence on W_{nr} and its value increases when W_{nr} decrease. Therefore, according to the above discussion, it was expected a decrease in lifetime values with the addition of silica. The lifetime τ of the level $^4I_{13/2}$ as a function of powder composition was measured and the results are listed in Table 2. Contrary to the expectation, no significant variation was observed ($\tau \sim 5$ ms). Therefore, there might be a competitive mechanism that comes into equilibrium with the nonradiative phonon-assisted relaxation. This mechanism was the result of up-conversion effect.

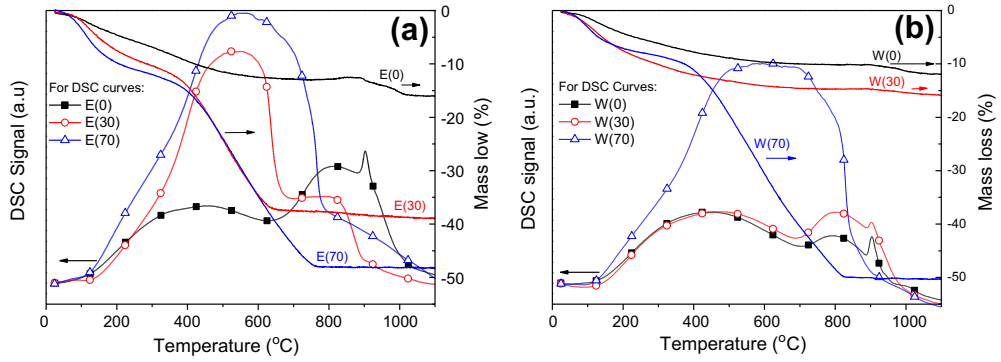

Fig. 5. TG-DSC analysis curves for powders pre-treated at 400 °C using (a) ethanol and (b) water as solvent, considering different concentrations of silica for each case.

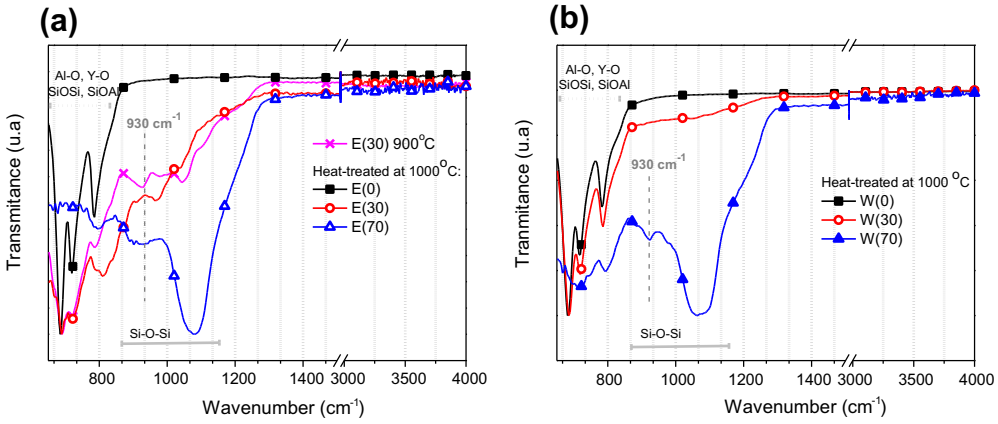

Fig. 6. FT-IR spectra of powders (considering $x = 0$, 30 and 70) heat-treated at 1000 °C for (a) ethanol and (b) water used as solvent. The spectrum of E(30) 900 °C was also considered.

Fig. 7 shows the up-conversion spectra dependence on x considering the temperatures that optimized the intensity at 1540 nm ($T = 900$ °C for ethanol and $T = 1000$ °C for water). To associate with PL results, the I_{max} values as a function of x, for each solvent, are shown in the insets of this figure.

The spectra are divided into two parts: green emission, in the range of 520–570 nm (due to $^2H_{11/2} + {}^4S_{3/2} \rightarrow {}^4I_{15/2}$) and red emission, in the range of 640–685 nm (due to $^4F_{9/2} \rightarrow {}^4I_{15/2}$). The proposed up-conversion channels are illustrated in the energy level diagram of Fig. 8 [21,22]. These up-conversion mechanisms are intensely affected by the excited-state absorption (ESA) and energy transfer (ET) between Er^{3+} ions [23,24]. ET process is strongly dependent on the dispersion of the ions in the host. Firstly, upon 980 nm excitation, the levels $^4I_{11/2}$ and $^4I_{13/2}$ are populated after the ground-state absorption (GSA) process. For green Er^{3+} emissions, a second step excitation of $^4I_{11/2}$ level can occur by ESA or ET mechanisms, represented schematically as follows:

$$ESA_{green} : {}^4I_{11/2} + \text{photon}(980\ \text{nm}) \rightarrow {}^4F_{7/2}$$

$$ET_{green} : {}^4I_{11/2} + {}^4I_{11/2} \rightarrow {}^4F_{7/2}$$

Than,

$$^4F_{7/2} \xrightarrow{\text{nonradiative relaxation}} {}^2H_{11/2} + {}^4S_{3/2} \xrightarrow{\text{Radiative decay}} \text{photon}(520\ \text{nm}) + \text{photon}(540\ \text{nm})$$

For the red emission, the second excitation occurs at the $^4I_{13/2}$ level, also by ESA and ET mechanisms as follows:

$$ESA_{red} : {}^4I_{13/2} + \text{photon}(980\ \text{nm}) \rightarrow {}^4F_{9/2}$$

$$ET_{red} : {}^4I_{13/2} + {}^4I_{11/2} \rightarrow {}^4F_{9/2}$$

Than,

$$^4F_{9/2} \xrightarrow{\text{Radiative decay}} \text{photon}(640 - 685\ \text{nm})$$

The alternative mechanisms that populate the $^4F_{9/2}$ are non-resonant and, as a consequence, would appreciably depend on the host.

Fig. 7(a) shows that only green emission was observed, which intensity decreased with the increase of silica content. In this figure, the spectra for $x \geq 50$ were not presented, due to the low intensity of the effect. However, Fig. 7(b) exhibits up-conversion effect with higher intensity and with more pronounced peaks. Both green and red emissions were observed for values of x up to 60. The addition of silica was followed by the decrease of the green emission intensity. On the other hand, red emission did not show a systematic dependence on x and was more evident for $x = 60$. As the red emission is the result of energy loss toward the host, we could infer that the interaction of Er^{3+} with the host was higher when water was used as the solvent.

To explain the observed variations on I_{max} and the almost constant values of τ as a function of x, we could infer that there was two

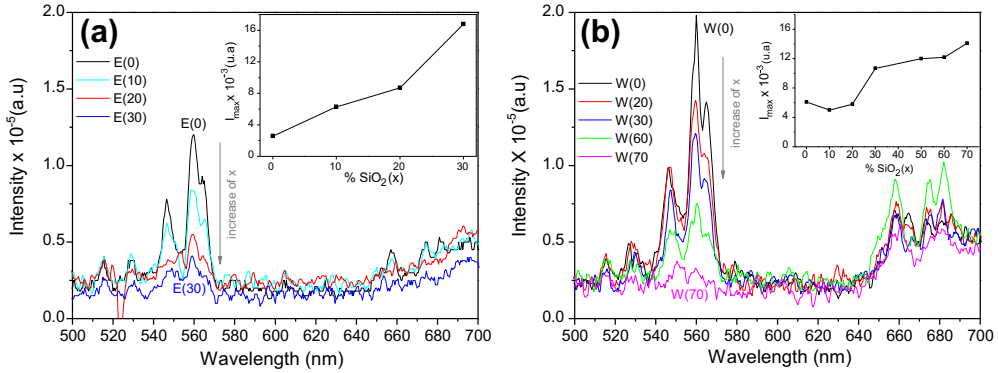

Fig. 7. Up-conversion emission spectra dependence with x of (a) E($x = 0$–30) 900 °C and (b) W($x = 0$–70) 1000 °C powders. These spectra were recorded at room temperature upon excitation of 980 nm. To associate with PL results, the insets show the PL emission intensity at 1540 nm (I_{max}) as a function of the silica content (x).

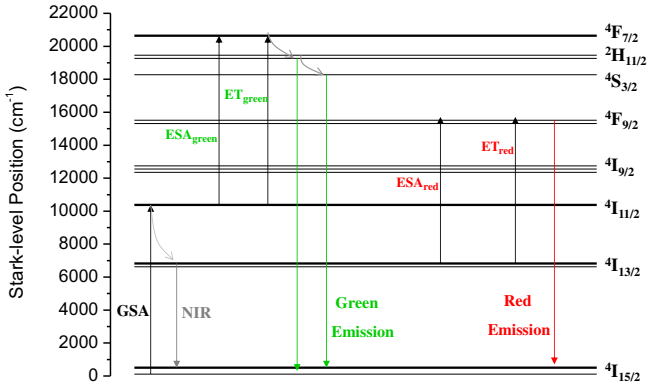

Fig. 8. Energy level diagram of Er^{3+}. Up-conversion mechanisms by excited-state absorption (ESA) and energy transfer (ET) are shown for green and red emissions, upon excitation at 980 nm [22]. (For interpretation of the references to color in this figure legend, the reader is referred to the web version of this article.)

competitive effects: (i) nonradiative phonon-assisted relaxation and (ii) up-conversion effect, resulting from ion–ion interaction. Both significantly affected the values of lifetime, I_{max} and FWHM. From the insets of Fig. 7, it is interesting to note, for both water and ethanol, as lower as the up-conversion effect, higher is the emission at 1540 nm.

Summarizing, the addition of silica played an important role on increasing the dispersion and solubility of Er^{3+} ions in the semi-crystalline samples, which resulted in a reduction of ion–ion interaction and an increase of PL intensity at 1540 nm. The FT-IR result associated to the appearance of non-bridging oxygen groups at the optimal conditions of x and T (Section 3.3) ensured this idea. Some authors reported that the non-bridging oxygen groups can reduce the tendency of Er^{3+} ions to cluster [25,26], improving the rare-earth solubility and PL intensity.

4. Conclusions

Powders with $(100 - x)\ Y_3Al_5O_{12} - (x)\ SiO_2$ compositions were synthesized by a modified Pechini method in order to find a host that optimizes the emission of erbium ions at 1540 nm. The role of SiO_2 concentration on the host properties was emphasized, considering ethanol and water as the solvent in the resin preparation process. In the optimization process, two effects were evaluated (i) the broadening of the PL spectrum associated to the crystal field symmetry at the Er^{3+} site, (ii) the increase of the dispersion of Er^{3+} ions with reduction of ion–ion interaction resulting in the increase of PL intensity. These effects have proved to be strongly dependent on a list of variables: crystallinity, secondary phases, highest phonon energy, lifetime, appearance of non-bridging oxygen groups and loss of energy by up-conversion and other non-radiative mechanism. All these variables were evaluated as a function of the silica content and temperature. The highest emission intensity at 1540 nm was observed in E(30) 900 °C and W(70) 1000 °C powders. It is important to note that the optimal conditions for ethanol solvent are quite different for water used as the solvent, confirming that the PL properties at the NIR region are highly sensitive to the changes in the host stoichiometry and processing conditions.

Acknowledgments

We would like to acknowledge the financial support from CAPES and CNPq.

References

[1] A. Polman, Erbium implanted thin film photonic materials, J. Appl. Phys. 82 (1) (1997) 1–39.
[2] B.R. Judd, Optical absorption intensities of rare-earth ions, Phys. Rev. 127 (1962) 750–761.
[3] R.M. Moon, W.C. Koehler, H.R. Child, L.J. Raubenheimer, Magnetic structures of Er_2O_3 and Yb_2O_3, Phys. Rev. 176 (2) (1968) 722–731.
[4] R.J. Mears, L. Reekie, I.M. Jauncey, D.N. Payne, Low-noise Erbium-doped fiber amplifier operating at 1.54 μm, Electron. Lett. 23 (19) (1987) 1026–1028.
[5] C. Duverger, M. Montagna, R. Rolli, S. Ronchin, L. Zampedri, M. Fossi, S. Pelli, G.C. Righini, A. Monteil, C. Armellini, M. Ferrari, Erbium-actived silica xerogels: spectroscopic and optical properties, J. Non-Cryst. Solids 280 (1–3) (2001) 261–268.
[6] M.L. Baesso, A.C. Bento, L.C.M. Miranda, D.F. de Souza, J.A. Sampaio, L.A.O. Nunes, Rare-earth doped low sílica calcium aluminosilicate glasses for near and mid infrared applications, J. Non-Cryst. Solids 276 (2000) 8–18.
[7] Y. Mizutani, H. Yasuda, I. Ohnaka, Y. Waku, Phase selection of the Al2O3–Y2O3 system controlled by nucleation, Mat. Trans. 42 (2) (2001) 238–244.
[8] M. Kakihana, M. Yoshmura, Synthesis and characteristics of complex multicomponent oxides prepared by polymer complex method, Bull. Chem. Soc. Jpn. 72 (7) (1999) 1427–1443.
[9] J. Lin, M. Yu, C. Lin, X. Liu, Multiform oxide materials via the versatile Pechini-type sol–gel process: synthesis and characteristics, J. Phys. Chem. C 111 (16) (2007) 5835–5845.
[10] B.T. Stone, K.L. Bray, Fluorescence properties of Er^{3+}-doped sol–gel glasses, J. Non-Cryst. Solids 197 (2–3) (1996) 136–144.
[11] L.C. Klein, Sol–gel processing of silicates, Annu. Rev. Mater. Sci. 15 (1985) 227–248.
[12] D. Ning, Y. lv-yun, P. Ming-ying, Z. Qing-ling, C. Dan-ping, T. Akai, K. Kadono, Preparation and spectroscopic properties of Er3+-doped high silica glass fabricated by sintering nanoporous glass, Mater. Lett. 60 (2006) 1987–1989.
[13] P. Jander, W.S. Brocklesby, Spectroscopy of yttria–alumina–silica glass doped with thulium and erbium, IEEE J. Quantum Electron 40 (5) (2004) 509–512.
[14] P.T. Nga, C. Barthou, P. Benalloul, P.N. Thang, L.N. Chung, P.V. Hoi, L.V. Luat, P.T. Cuong, Effects of yttrium codoping on fluorescence lifetimes of Er^{3+} ions in SiO_2–Al_2O_3 sol–gel glasses, J. Non-Cryst. Solids 352 (2006) 2385–2389.
[15] S. Chen, C. Ting, C. Li, Fluorescence enhancement and structural development of sol–gel derived Er^{3+}-doped SiO_2 by yttrium codoping, J. Mater. Chem. 12 (2002) 1118–1123.
[16] I. Muliuoliene, S. Mathur, D. Jasaitis, H. Shen, V. Sivakov, R. Rapalaviciute, A. Beganskiene, A. Kareiva, Evidence of formation of mixed-metal garnets via sol–gel synthesis, Opt. Mater. 22 (3) (2003) 241–250.
[17] S. Aasland, P.F. Mcmillan, Density-driven liquid-liquid phase separation in the system Al_2O_3–Y_2O_3, Nature 369 (1994) 633–636.
[18] E. De la Rosa, L.A. Díaz-Torres, P. Salas, A. Arredondo, J.A. Montoya, C. Angeles, R.A. Rodríguez, Low temperature synthesis and structural characterization of nanocrystalline YAG prepared by a modified sol–gel method, Opt. Mater. 27 (12) (2005) 1793–1799.
[19] M. Sroda, Cz. Paluszkiewicz, The structural role of alkaline earth ions in oxyfluoride aluminosilicate glasses – infrared spectroscopy study, Vib. Spectrosc. 48 (2) (2008) 246–250.
[20] J.T. Kohli, R.A. Condrate, J.E. Shelby, Raman and infrared of rare earth aluminosilicate glasses, Phys. Chem. Glasses 34 (3) (1993) 81–87.
[21] V.D. Rodríguez, J. Del Castillo, A.C. Yanes, J. Méndez-Ramos, M. Torres, J. Peraza, Luminescence of Er^{3+}-doped nanostructured SiO_2–LaF_3 glass–ceramics prepared by the sol–gel method, Opt. Mater. 29 (2007) 1557–1561.
[22] C. Xie, Z. Yang, Y. Sun, Synthesis and characterization of monodispersed SiO_2@$Y_3Al_5O_{12}$: Er^{3+} core–shell particles, J. Fluoresc. 19 (2009) 623–629.
[23] S. Ann, Upconversion excitation of green fluorescence in Er:YAG, J. Lumin. 60-61 (1994) 636–639.
[24] S. Georgescu, O. Toma, I. Ivanov, Upconversion from the $^4I_{13/2}$ and $^4I_{11/2}$ levels in Er:YAG, J. Lumin. 114 (2005) 43–52.
[25] K. Arai, H. Namikawa, K. Kumata, T. Honda, Y. Ishii, T. Handa, Aluminum or phosphorous co-doping effects on the fluorescence and structural properties of neodymium-doped silica glass, J. Appl. Phys. 59 (1986) 3430–3436.
[26] Y. Zhou, Y.L. Lam, S.S. Wang, H.L. Liu, C.H. Kam, Y.C. Chan, Fluorescence enhancement of Er^{3+}-doped sol–gel glass by aluminum codoping, Appl. Phys. Lett. 71 (5) (1997) 587–589.